


Article

Thermal Finite-Element Model of Electric Machine Cooled by Spray

Christian Bergfried^{1,2,*}, Samaneh Abdi Qezeljah^{2,3} , Ilia V. Roisman³, Herbert De Gersem^{1,2,*} ,
Jeanette Hussong^{2,3}  and Yvonne Späck-Leigsnering^{1,2} 

¹ Institute for Accelerator Science and Electromagnetic Fields (TEMF), Technische Universität Darmstadt, 64289 Darmstadt, Germany

² Graduate School of Excellence Computational Engineering (CE), Technische Universität Darmstadt, 64289 Darmstadt, Germany; abdi.qezeljah@sla.tu-darmstadt.de (S.A.Q.)

³ Institute for Fluid Mechanics and Aerodynamics (SLA), Technische Universität Darmstadt, 64289 Darmstadt, Germany

* Correspondence: christian.bergfried@tu-darmstadt.de (C.B.); degersem@temf.tu-darmstadt.de (H.D.G.)

Abstract: The demand for higher power density in electrical machines necessitates advanced cooling strategies. Spray cooling emerges as a promising and relatively straightforward technology, albeit involving complex physics. In this paper, a quasi-3D thermal finite-element model of stator winding is created by the extrusion of a 2D cross-sectional finite-element model along the winding direction. The cooling effects of the spray impact are simulated as a heat flux that uses an impedance boundary condition at the surface of the winding overhang. The results confirm the advantageous performance of spray cooling, indicating that it may enable a tenfold increase in power density compared to standard air- or water-cooled machines.

Keywords: spray cooling; finite-element method; quasi-3D; thermal model



Academic Editors: Sławomir Dykas and Luigi Fortuna

Received: 25 November 2024

Revised: 19 December 2024

Accepted: 26 December 2024

Published: 28 December 2024

Citation: Bergfried, C.; Abdi Qezeljah, S.; Roisman, I.V.; De Gersem, H.; Hussong, J.; Späck-Leigsnering, Y. Thermal Finite-Element Model of Electric Machine Cooled by Spray. *Energies* **2025**, *18*, 84. <https://doi.org/10.3390/en18010084>

Copyright: © 2024 by the authors. Licensee MDPI, Basel, Switzerland. This article is an open access article distributed under the terms and conditions of the Creative Commons Attribution (CC BY) license (<https://creativecommons.org/licenses/by/4.0/>).

1. Introduction

Electric machines produce heat due to electrical losses and mechanical friction. These losses are especially pronounced during startup or dynamic braking and tend to increase significantly with heavier loads. Excessive heat can reduce machine efficiency and eventually lead to failure. This is why proper cooling of the electric machine parts is necessary to ensure that the machine operates at optimal temperatures, preventing overheating, which can lead to possible subsequent damage. Overheating can harm electronic components and shorten the machine's lifespan. High-speed electric machines face challenges due to higher loss densities. A thorough thermal analysis, combined with electromagnetic and mechanical considerations, as well as appropriate cooling processes, is essential during design [1–3]. Several traditional cooling methods, such as with water-cooling jackets, oil, and air cooling, have been widely investigated in automotive applications [4,5]. Efficient cooling of high-power density electric machines is a rather challenging problem [6–10] that cannot be easily solved using these conventional approaches.

Recently, spray cooling has started to be considered by engineers as a potentially very efficient technology for improving the thermal control of electric machines and other powerful electric and electronic systems [11]. Experiments on the thermal management of electric machines are usually focused on cooling the end winding [12–15], which is a relatively easily accessible and intensively heated part of the machine (Figure 1). The application of multiple full-cone nozzles [12] is recommended for achieving uniform cooling.

In most cases, cooling the winding requires some effort to prevent the flow of the aerosol of the oil from dropping into the gap between the stator and rotor [16]. Nonetheless, some recent studies suggest using air/spray cooling, including for winding and gap cooling of the electric machine [17]. The application of spray cooling to the thermal management of electric machines has also been investigated using computational fluid dynamics (CFD) computation based on existing empirical models from the literature, and, in some cases, it shows improvement according to experimental estimations of the heat flux [18–20]. In all these studies, several important parameters are missing. First and foremost, the spray used for cooling is not properly characterized. The average drop diameter (for example, the Sauter mean diameter D_{32}), the average drop velocity and direction, the local mass flux density, and the temperature are the main parameters influencing spray cooling. These parameters are often measured using phase Doppler instruments [21] or other optical methods [22]. The heat flux is also determined by the thermal and rheological properties of the liquid as well as the surface and thermal properties of the substrate. This is why, for the sake of a more accurate model, it is important to understand the basic dynamics of the drop, spray impact, and accompanying heat transfer occurring in spray cooling applications. Spray impingement is a very effective means of removing heat from hot surfaces. Spray cooling processes are used in the field of metal production [23,24], for cooling high-power electronic devices, data centers, and hybrid electric vehicles [25,26], for cooling laser diode scanners [27], in aerospace applications [28], and for cryogenic cooling of human tissue in medicine [29] and other biomedical applications [30]. The advantage of spray cooling lies in the simplicity of its technical realization. The ability to direct the spray allows for covering a large cooling area. These advantages are complemented by the ability to provide relatively high heat fluxes comparable with those produced by micro-channels, heat pipes, or other high-intensity heat removal technologies. Comprehensive literature reviews on spray cooling in various systems and the physical phenomena involved can be found in [31–33]. Spray impact onto a solid substrate quickly forms a thin, fluctuating liquid wall film. This film is generated by the deposited liquid after drop impacts. The dynamics of the film are governed by viscous and capillary effects, as well as by flow disturbances caused by drop impacts, as shown in Figure 2. This is why the phenomenon of spray impact cannot be modeled as a simple superposition of drop impact events [34]. This is also the reason why the modeling approaches describing the deposition mass ratio and the characteristics of spray cooling are mainly empirical.

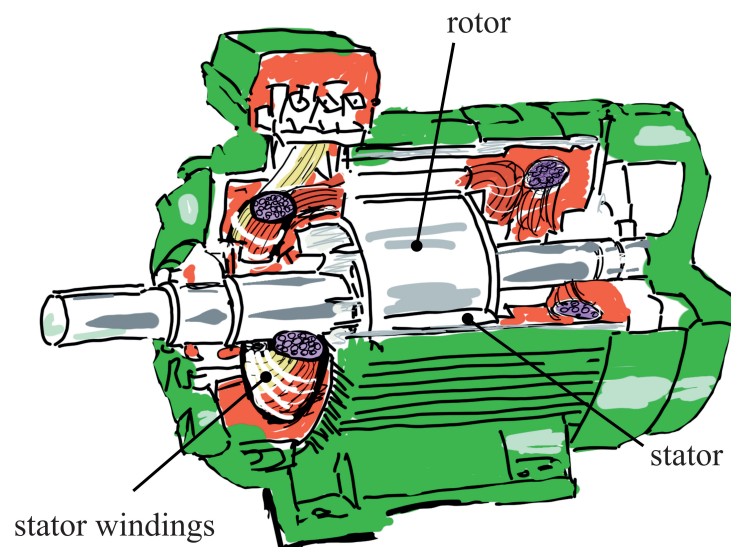


Figure 1. Schematic view of an electric machine.

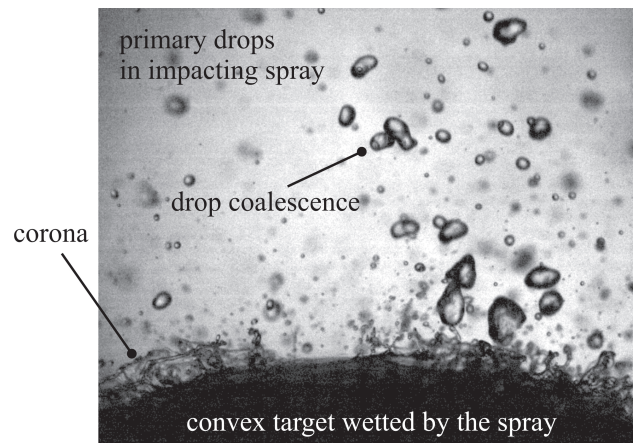


Figure 2. Shadowgraphy image of spray impact onto a convex solid target.

The outcome of a drop impact onto a wetted wall is determined by the material properties of the liquid, like density ρ , viscosity μ , surface tension σ , the thickness of the wall film h_{film} , impact velocity U_0 , impact angle, and initial drop diameter D_0 . The corresponding dimensionless quantities include the Reynolds and the Weber numbers and dimensionless film thickness

$$\text{Re} = \frac{\rho D_0 U_0}{\mu}, \quad \text{We} = \frac{\rho D_0 U_0^2}{\sigma}, \quad \delta = \frac{h_{\text{film}}}{D_0}. \quad (1)$$

Typical outcomes of a drop impact onto a wetted wall are shown in Figure 3. They include drop rebound at very small Weber numbers. Rebound is governed by the stresses in a thin air gap between the impacting drop and the liquid film, deposition, and formation of an uprising liquid sheet formed as a result of the interaction of the flow in the lamella with the outer undisturbed film. At velocities exceeding the splashing threshold, drop impact leads to the generation of a secondary drop: splash.

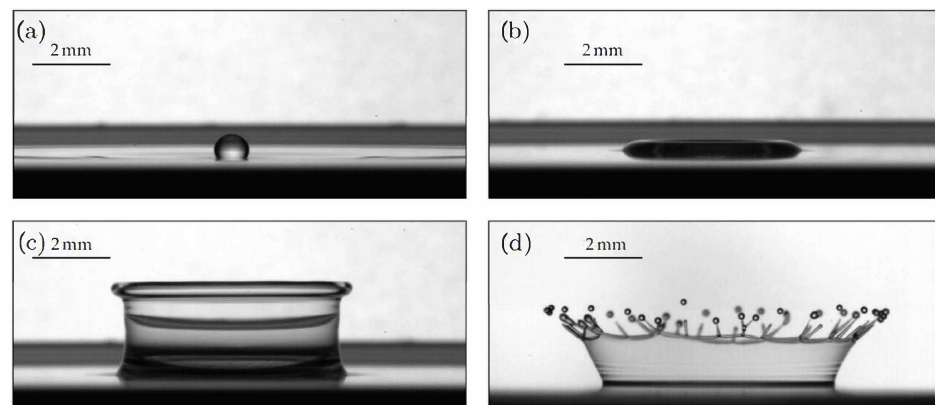


Figure 3. Typical outcomes of drop impact onto a wetted substrate: (a) Floating/bouncing ($We = 0.62$, $Re = 24$, $\delta = 0.33$); (b) Deposition ($We = 78$, $Re = 300$, $\delta = 0.33$); (c) Crown formation ($We = 700$, $Re = 900$, $\delta = 0.33$); (d) Splash ($We = 1224$, $Re = 604$, $\delta = 0.04$).

The splash is also the result of various hydrodynamic phenomena. Typical splash phenomena, i.e., prompt splash, corona splash, corona detachment, and breakup of a central jet, are shown in Figure 4. Among the important results of drop impact studies [35] are the splashing threshold [36,37]

$$K_{\text{splash}}^{8/5} = 2100 + 5800\delta^{1.44}, \quad K \equiv \text{We}^{1/2}\text{Re}^{1/4}, \quad (2)$$

and the splashed mass ratio

$$\eta_{\text{splashed mass}} \approx 0.5 - 0.62 \exp[-K_{\text{primary}}^{8/5}], \tag{3}$$

where K_{primary} is the averaged K - number, defined in (2), which is computed using the averaged parameters of the primary spray before wall impact. The corresponding deposited mass ratio is therefore

$$\eta_{\text{deposited mass}} = 1 - \eta_{\text{splashed mass}} \tag{4}$$

since the mass lost due to evaporation during the short time of drop collision is relatively small.

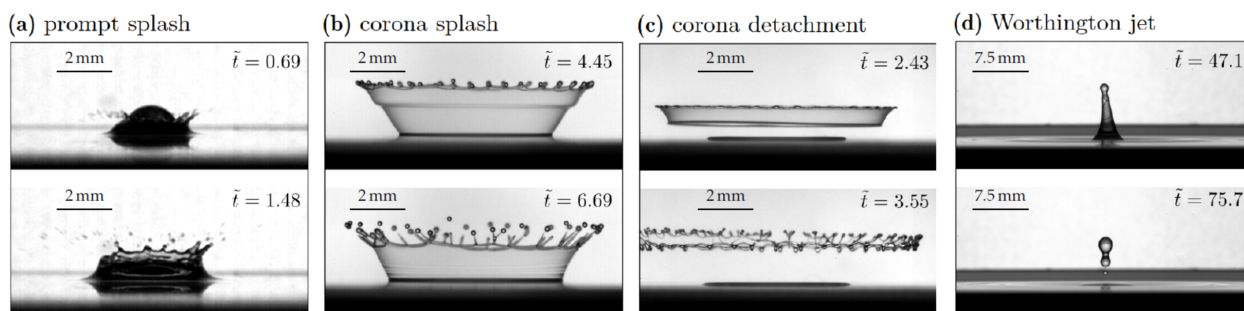


Figure 4. Various types of splash observed in experiments: (a) Prompt splash; (b) Corona splash; (c) Corona detachment; (d) Worthington jet.

The outcome of drop impact can also be significantly influenced by temperature, as shown in the example in Figure 5. This result can be explained by the dependence of viscosity and surface tension on temperature, as well as by the emergence of forces associated with thermal Marangoni effects or even liquid boiling. The model for heat flux associated with spray cooling depends on wall temperatures and, thus, on the impact of hydrodynamic and thermodynamic regimes. These regimes, at the highest wall temperatures, include drop rebound due to film boiling or drop thermal atomization. At intermediate temperatures, which still significantly exceed the boiling temperature, drop impact is accompanied by intensive nucleate boiling. At lower temperatures below the boiling point, heat transfer occurs mainly by convection in the drop and in the liquid film and by heat conduction in the substrate in the expanding thermal boundary layers.

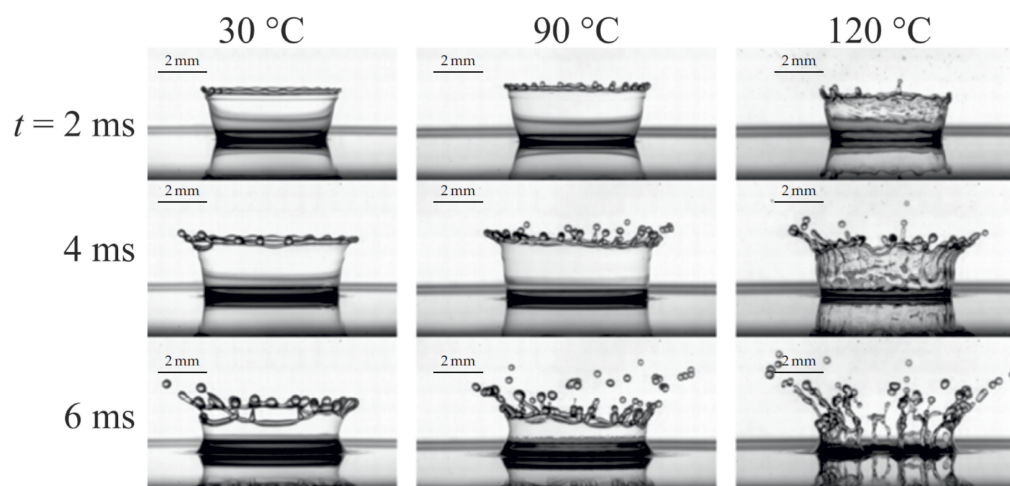


Figure 5. Effect of liquid temperature on the outcome of a Hexadecane drop impacting onto a Hexadecane wall film with $\delta = 0.1$, $D_0 = 2$ mm, and $U_0 = 3$ m/s.

For relatively low temperatures, typical of the operating conditions of electric devices, heat transfer is influenced by the expansion of a crater, which is formed in the film by

drop impact. Heat transfer depends on the residual film thickness at the bottom of a crater, which is determined by the viscous stresses [38,39], duration of the crater expansion, and the receding and maximum spreading diameter.

This paper focuses on the simulation of heat extraction from winding overhang. The heat transfer coefficient is determined from an experiment (Section 5), which included various volumetric fluxes, drop velocities, and diameters. In contrast to the CFD simulations in [18–20], the finite-element (FE) method is applied, with the assumption of a uniformly distributed spray [12]. Additionally, a quasi-3D approach is exploited, which is successfully used in other physical simulations as in [40–42] while avoiding an unaffordable three-dimensional (3D) simulation.

2. Thermal Model

2.1. Thermal Machine Model

During electric machine operation, there are several sources of heat. In the stator and rotor windings and bars, Joule losses are generated. In the yoke parts, eddy-current and hysteresis losses are generated. At the interface between moving parts, friction losses occur. A stator winding consists of wires separated by insulation. A part is mounted in the stator slots. The overhang winding parts stick out at the front and back sides of the machine. The interturn insulation is considered one of the weakest parts of an electric machine [43] and is, therefore, a common reason for machine failures. This paper will focus on the cooling of the stator windings and thus consider the Joule losses as the major heat source. The inside parts of the stator windings are hot spots. Commonly, the heat is extracted from the overhang winding parts by air cooling. In this paper, spray cooling of the overhang winding parts is studied as an alternative.

As an example machine model, a squirrel-cage induction machine located at the Electric Drives and Power Electronic Systems Institute of TU Graz is considered [44]. Its thermal properties have been investigated in [45,46]. The machine is designed for a nominal power of 3.7 kW at a nominal speed of 1430 rpm. Moreover, it is rated for air-cooling but is surrounded by a cooling jacket for measurement purposes.

2.2. Heat Conduction Model

In the stationary case, the heat equation [47] is

$$-\nabla \cdot (\lambda \nabla \vartheta) = p, \quad \text{in } \mathcal{V} \subset \mathbb{R}^3; \quad (5)$$

$$\vartheta = \vartheta_{\text{iso}}, \quad \text{at } \mathcal{S}_{\text{iso}}; \quad (6)$$

$$\vec{n} \cdot \vec{q} = 0, \quad \text{at } \mathcal{S}_{\text{adia}}; \quad (7)$$

$$\vec{n} \cdot \vec{q} = g_{\text{imp}}(\vartheta), \quad \text{at } \mathcal{S}_{\text{imp}}, \quad (8)$$

where $\vartheta(\vec{r})$ is the temperature, $\vec{q}(\vec{r}) = -\lambda \nabla \vartheta$ is the heat flux density, $\lambda(\vec{r}, \vartheta(\vec{r}))$ is the thermal conductivity, and $p(\vec{r})$ is the internal heat source density; in the case of a stator winding, it is the Joule loss density. V is the computational domain, $\partial V = \mathcal{S}_{\text{iso}} \cup \mathcal{S}_{\text{adia}} \cup \mathcal{S}_{\text{imp}}$ its surface divided into an isothermal, adiabatic, and impedance part, $\vec{n}(\vec{r})$ is the unit normal vector at ∂V and $\vec{r} = (x, y, z)$ is the coordinate system, where z is the direction along the axis of the machine.

The isothermal boundary condition (BC) enforces a prescribed temperature distribution ϑ_{iso} at \mathcal{S}_{iso} . The adiabatic BC prescribes the heat flux density, here 0. The impedance BC imposes a relation g_{imp} between heat flux density and the temperature at the boundary.

2.3. Simplification of the Thermal Model

To reduce model complexity and computational effort, the following assumptions are considered:

- The problem is stationary: This assumes a constant internal and external heat source density. As a consequence, the heat generated in the domain equals the heat flux through the surface.
- The radial heat flux within the machine is negligible: This implies that the generated heat within the stator winding flows toward the overhang winding, and is there removed by spray cooling.
- The properties of the spray cooling are constant, i.e., the liquid film has a constant thickness and a constant temperature.
- The central part of the geometry is invariant in z -direction. The problem is formulated for the 2D cross-section of the machine. Nevertheless, some field features are axial dependent, which will be taken into account by a quasi-3D formulation.
- To model the spray cooling effects, the machine model gets reduced to a stator winding.

With these assumptions, the thermal model gets reduced to

$$-\nabla \cdot (\lambda \nabla \vartheta) = p, \quad \text{in } \Omega_k; \quad (9)$$

$$-\lambda \nabla \vartheta \cdot \vec{n} = 0, \quad \text{at } \Gamma_{\text{adia}}; \quad (10)$$

$$\lambda \nabla \vartheta \cdot \vec{n} + h(\vartheta - \vartheta_0) = 0, \quad \text{at } \Gamma_{\text{imp}}, \quad (11)$$

with

$$\Omega_k := \{\vec{r} = (x, y, z) \in \mathcal{V} \mid z = f(s)\} \quad \text{for } k \leq |N| \in \mathbb{Z};$$

$$\Gamma_{\text{adia}} := \{\vec{r} = (x, y, z) \in \partial\Omega_k \cap \mathcal{S}_{\text{adia}}\} \quad \text{for } k < \left\lfloor \frac{3}{5}N \right\rfloor \in \mathbb{Z};$$

$$\Gamma_{\text{imp}} := \{\vec{r} = (x, y, z) \in \partial\Omega_k \cap \mathcal{S}_{\text{imp}}\} \quad \text{for } k > \left\lfloor \frac{3}{5}N \right\rfloor \in \mathbb{Z};$$

where Ω_k are discrete cross-sections of \mathcal{V} , Γ_{imp} and Γ_{adia} are the boundaries. h is the heat transfer coefficient at Γ_{imp} modeling the spray cooling at the overhang winding surface. The field problem is solved with the FE solver Pyrit [48] and validated using COMSOL Multiphysics® [49]. The heat source density equals the Joule losses [50]

$$p = \frac{J^2}{\sigma_{\text{cu}}}, \quad (12)$$

where J is the current density and σ_{cu} is the electric conductivity of copper.

3. Discretization

The assumption of a translatory invariant geometry in the winding direction allows for a two-dimensional (2D) cross-sectional FE model, which is extruded in the winding direction using the quasi-3D approach.

3.1. Finite-Element

The 2D cross-section is meshed with triangles. The temperature is approximated as

$$\vartheta \approx \sum_{j=1}^N u_j N_j \quad (13)$$

where $N_j(x, y)$ are 2D first-order nodal shape functions and u_j the degrees of freedom.

Using the Ritz-Galerkin approach [51], the thermal model (9) leads to the system of equations

$$(\mathbf{K}_\lambda + \mathbf{M}_h)\mathbf{u} = \mathbf{p} + \mathbf{q} \quad (14)$$

with the stiffness matrix \mathbf{K}_λ , the mass matrix \mathbf{M}_h and the internal load vector \mathbf{p} and external load vector \mathbf{q} expressed.

$$K_{\lambda,ij} = \int_{\Omega} \lambda \nabla N_j \cdot \nabla N_i \, d\Omega; \quad (15)$$

$$M_{h,ij} = \int_{\Omega} h N_j N_i \, d\Omega; \quad (16)$$

$$p_i = \int_{\Omega} p N_i \, d\Omega; \quad (17)$$

$$q_i = \int_{\Gamma} h \vartheta_0 N_i \, d\Gamma. \quad (18)$$

3.2. Quasi-3D Approach

The winding direction is discretized by

$$z = f(s), \quad (19)$$

where $f(s)$ is a Frenet-Serret mapping [52]. For this, one-dimensional (1D) quadratic Lagrange shape functions $N_k^{1D}(z)$ are introduced as

$$N_1(\xi) = \frac{1}{2}\xi(\xi - 1), \quad (20)$$

$$N_2(\xi) = (1 - \xi^2), \quad (21)$$

$$N_3(\xi) = \frac{1}{2}\xi(\xi + 1). \quad (22)$$

Here, ξ is a reference 1D element with $\xi \in [-1, 1]$. Therefore, the approximation in (13) becomes the quasi-3D formulation

$$\vartheta(u, v, s) \approx \sum_{j=1}^N \sum_{k=1}^N u_{jk} N_j^{2D}(u, v) N_k^{1D}(s). \quad (23)$$

With this approximation of the temperature, the stiffness matrix \mathbf{K}^{3D} is derived as [40]

$$\begin{aligned} K_{\lambda,ijkl} &= \int_{\Omega} \lambda \nabla(N_j^{2D} N_k^{1D}) \cdot \nabla(N_i^{2D} N_l^{1D}) \, d\Omega; \\ &= \underbrace{\int_{\Omega} \lambda \nabla N_j^{2D} \cdot \nabla N_i^{2D} N_k^{1D} N_l^{1D} \, d\Omega}_{M_{kl}^{1D} \otimes K_{ij}^{2D}} \\ &\quad + \underbrace{\int_{\Omega} \lambda N_j^{2D} N_i^{2D} \nabla N_k^{1D} \cdot \nabla N_l^{1D} \, d\Omega}_{K_{kl}^{1D} \otimes M_{ij}^{2D}}. \end{aligned} \quad (24)$$

The 3D stiffness matrix \mathbf{K}^{3D} is constructed using 1D- and 2D-stiffness, K , and mass matrix, M , which are multiplied using the Kronecker product denoted as \otimes . A similar adjustment is necessary for the 3D mass matrix \mathbf{M}^{3D} and the loads \mathbf{q} and \mathbf{p}

$$M_{h,ijkl} = \int_{\Omega} \underbrace{h N_j^{2D} N_i^{2D} N_k^{1D} N_l^{1D}}_{M_{kl}^{1D} \otimes M_{ij}^{2D}} d\Omega, \quad (25)$$

$$q_{il}^{3D} = \int_{\Omega} \underbrace{h \theta_0 N_i N_l}_{q_i^{1D} \otimes q_l^{2D}} d\Omega, \quad (26)$$

$$p_{il}^{3D} = \int_{\Omega} \underbrace{p N_i N_l}_{p_i^{1D} \otimes p_l^{2D}} d\Omega. \quad (27)$$

4. Quasi-3D FE Model of a Stator Winding with Spray Cooling

4.1. Geometry

The winding model is displayed in Figure 6 as a 3D sketch and in Figure 7 as two cross-sections with different boundary conditions. Due to symmetry, it is sufficient to consider only a part of a single stator winding extending between the center cross-section of the machine ($z = 0$ in Figure 6a) to the outermost point of the overhang (point p in Figure 6a). The curved geometry is projected onto a straight (Figure 6b) by the coordinate transformation $(u, v, s) \rightarrow (x, y, z) = (f(u, v, s), g(u, v, s), h(u, v, s))$. To simplify the setting, u and v are chosen to match x and y in the center cross-sectional plane, and s is chosen to be the length measured along the center line of the winding. Moreover, the curvature torsion of the winding is neglected. These assumptions are acceptable for the thermal problem considered here but would not work for a magnetic model. In this simplified setting, a quasi-3D FE formulation of Section 3.2 can be applied without distinguishing between (u, v, s) and (x, y, z) .

The cross-section of the quasi-3D model is depicted in Figure 7. The area of the cross-section is 107.7 mm^2 , with two-layer wire windings immersed in insulating epoxy resin. Each layer consists of 18 copper wires, resulting in a copper fill factor of 59%. Other geometrical and thermal properties of the winding used in the computations are listed in Table 1.

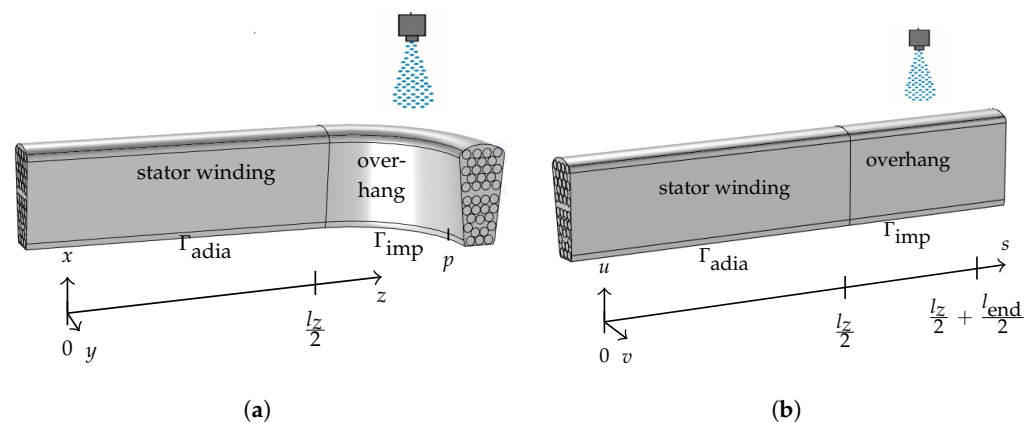


Figure 6. Simulation model of stator winding and overhang in different coordinate systems. (a) Cartesian coordinates; (b) Frenet-Serret coordinates.

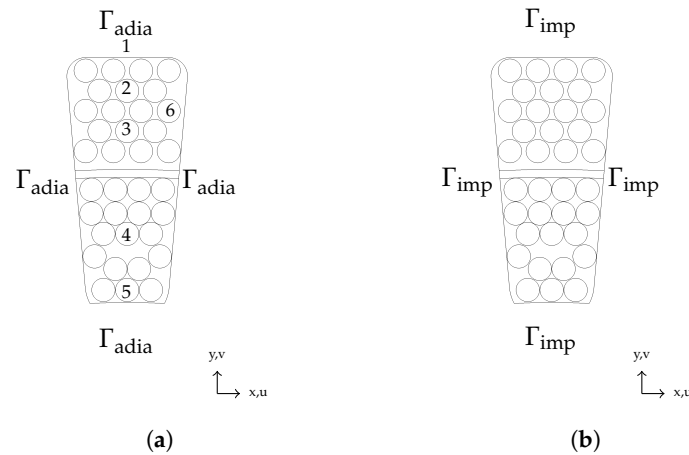


Figure 7. (a) 2D cross-section of the winding within the stator with the corresponding boundary conditions. The numbers indicate the points that are used for temperature evaluation. (b) 2D cross-section of the overhang-winding outside the stator. Only the overhang winding is getting spray-cooled.

Table 1. Parameters of the winding model.

Name	Parameter	Value	Unit
Length within stator	l_s	100	mm
Length overhang	l_{ew}	66.6	mm
Current density	J	10	A/mm ²
Electric conductivity copper	σ_{cu}	60	MS/m
Thermal conductivity copper	λ_{cu}	400	W/Km
Thermal conductivity insulation	λ_{ins}	0.7	W/Km
Thermal conductivity of water	λ_{film}	0.6	W/Km
Heat source density	p	1.7	MW/m ³

4.2. Boundary Condition

Due to symmetry, there is no heat flux through the center and outermost cross-sectional planes ($s = 0$ and $s = \frac{l_z}{2} + \frac{l_{end}}{2}$). Hence, adiabatic boundary conditions $-\lambda \frac{\partial \vartheta}{\partial s} = 0$ are applied there.

Within the stator yoke, the winding is surrounded by good electric insulation, which also provides good thermal insulation. As a consequence, the heat flux toward the stator yoke can be neglected. Hence, an adiabatic BC $-\lambda \frac{\partial \vartheta}{\partial s} = 0$ is applied (Figure 6a).

The winding overhang is subjected to spray cooling. It is assumed that the spray is homogeneously applied to the winding surfaces. The inhomogeneous temperature distribution, however, will cause inhomogeneous heat removal. The spray-cooling effect is modeled as an impedance BC $\vec{n} \cdot \vec{q} = g_{imp}(\vartheta) = h_{spray}(\vartheta - \vartheta_0)$ with $h_{spray} = 22,485$ W/Km² and $\vartheta_0 = 293$ K, as determined by the spray-cooling experiment reported below.

5. Experimental Characterization of the Spray Cooling

Figure 8 depicts an experimental setup [53] for studying spray impact onto a hot target and measuring the heat flux for various spray parameters: volumetric flux, drop velocity, and diameter. The setup consists of the following major sub-systems: a liquid supply system and atomizer for water spray generation, a convex target with a heating and thermal control system, and the observation system, which includes a high-speed video system with 16,000 fps (FASTCAM SA1, Photron, Reutlingen, Germany) and high-speed infrared system with 100 frames at 244 Hz (Phoenix, Indigo Systems, FLIR Systems Inc. Santa Barbara, CA, USA). The spray has been characterized using a phase Doppler instrument. The heat flux in the target was measured using an array of thermocouples. The metal target of convex shape included a carefully calibrated thin thermal resistance layer parallel to the interface. This

allows a significant increase in the temperature jump in the thermocouple measurements and thus improves the precision of the heat flux measurements. The flow on the target surface is characterized by a high-speed infrared camera (see Figure 9) and a high-speed camera (see e.g., in Figure 2). The average film thickness at the generatrix of a convex target surface was measured using a high-resolution video camera with 36,000 fps (High-SpeedStar 5, LaVision, Göttingen, Germany). The experimental setup has been developed for investigating the effect of gravity acceleration on the heat flux associated with spray impact [54]. In this study, however, only results obtained under normal terrestrial conditions are relevant. The Sauter mean diameter D_{32} of the drops in the spray was varied from 390 to 890 μm , the average impact velocity was chosen in the range between 5.6 and 14 m/s, and the volumetric flow rate of the liquid was specified between 0.25 and 0.65 L/min. The spray angle is 30° , and the distance to the target is 70 mm. Therefore, the mass flux \dot{m} can be roughly estimated from the mass balance and geometrical considerations to be between 3.8 and 9.8 $\text{kg}/\text{m}^2\text{s}$. Interestingly, for these relatively wide ranges of the main spray parameters, the variations of the measured heat transfer coefficients h_{spray} are rather weak: from 2.2×10^4 to 2.3×10^4 $\text{W}/\text{m}^2\text{K}$. Hence, the dependencies of the spray-cooling effect on the spray-cooling parameters are neglected in the FE simulations reported below. A representative setting of the spray-cooling has been selected, for which the parameters, among the heat transfer coefficient h_{spray} and the environmental temperature used in the simulations, are listed in Table 2.

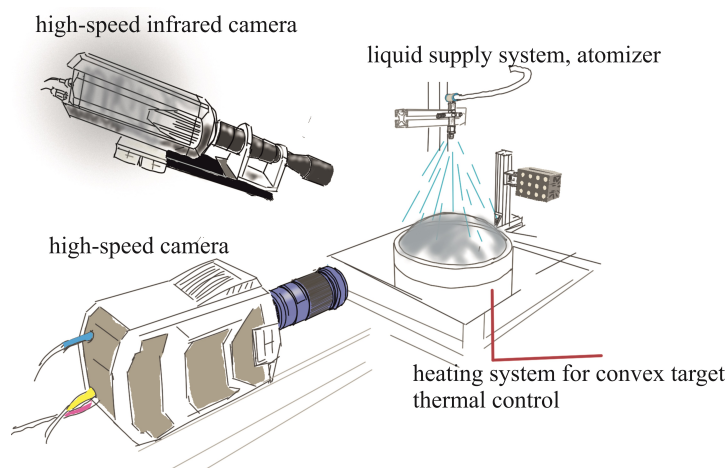


Figure 8. Sketch of the experimental setup used to investigate spray cooling. More details can be found in [53].

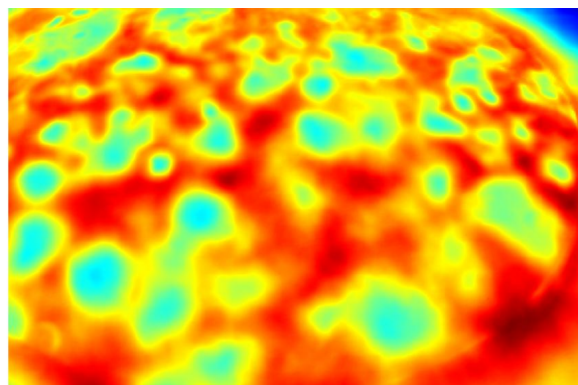


Figure 9. Spray-cooled target captured with an infrared camera. Red and yellow regions correspond to hot water film covering the target. Light blue and turquoise regions correspond to locations of recent impingement of cold droplets.

Table 2. Parameters used for computations.

Name	Parameter	Value	Unit
Mass flow rate	\dot{M}	0.35	kg/min
Estimated mass flux	\dot{m}	5.3	kg/m ² s
Average spray velocity	U_{spray}	7.77	m/s
Sauter mean diameter	D_{32}	497	μm
Spray temperature	ϑ_0	293	K
Film thickness	H_{film}	91	μm
Heat transfer coefficient	h_{spray}	22.5	kW/Km ²

6. Results and Discussion

6.1. Existing Machine

In the central cross-section, the maximal temperature difference is 0.5 K. Moreover, the individual wire cannot be recognized because the temperature distribution is almost homogeneous (see Figure 10 lower left corner). In the most outside cross-section, displayed in Figure 11, the temperature difference is 3 K from the winding center to the surface. Moreover, each wire is visible as a temperature gradient from the center to the surface exists.

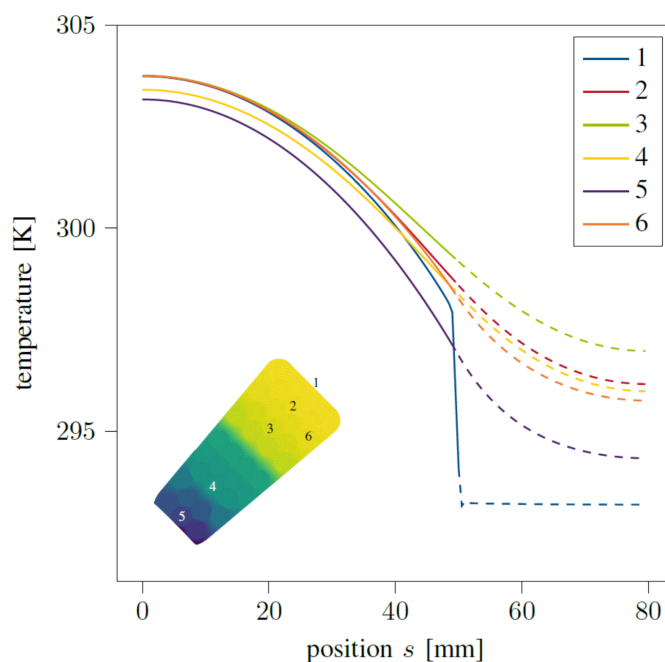


Figure 10. Temperature along the winding at six positions (1–6) within the winding's cross-section. The solid line represents the temperature in the winding inside the slot and the dashed line represents the temperature in the overhang part of the winding. To obtain the results for an entire winding, the result should be mirrored several times at the left and right positions.

The resulting temperature distribution along the winding direction is shown in Figure 10 for the temperature at selected points. The temperature distribution along the wire winding can be retrieved by mirroring the curves in Figure 10 left and right. Therefore, the position ($s = 0$ mm) is in the middle of the stator, the position ($s = \frac{l_z}{2} = 50$ mm) is the end of the stator and the beginning of the overhang, and the position ($s = \frac{l_z}{2} + \frac{l_{\text{end}}}{1} = 80$ mm) is the middle of the overhang. At the center cross-section (at 0 mm), the temperature in the center and at the surface are almost identical. This is attributed to the good thermal insulation between the winding and yoke. A temperature drop of 6 K is located at the end of the stator and at the beginning of the overhang. From the center cross-section, the temperature decreases continuously in the winding direction. The highest temperature

is in the lower layer of the winding, with 304 K within the slot and 296 K in the overhang. As this is the point with the largest distance to the surface, the cooling effect of the spray is the lowest there. The lowest temperature is found at the surface with the spray impact. It is only marginally larger than the spray temperature. Even within the center cross-section, where the winding is not cooled, the temperature of the wires remains at a moderate level. This is because the investigated machine is rated for air cooling.

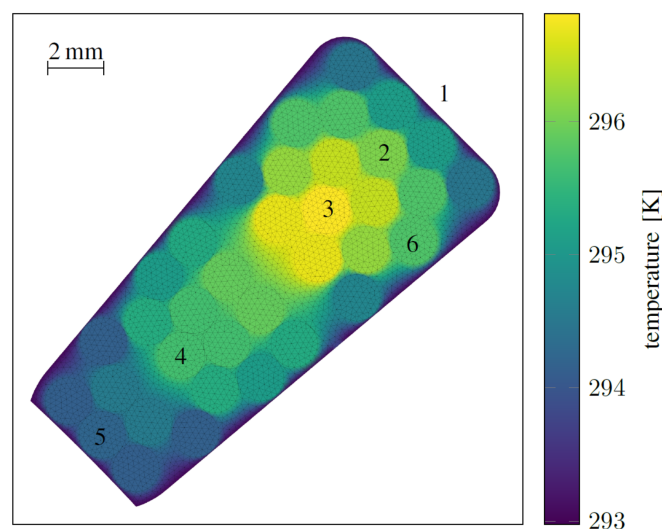


Figure 11. Temperature at six positions (1–6) within the winding’s cross-section at the most outside point ($s = \frac{l}{2} + \frac{l_{\text{end}}}{2}$). The distribution is mainly influenced by the spray-cooling boundary condition.

6.2. Machine with Increased Power Density

In machines with a higher power density, the effects of spray cooling will have a greater impact. To illustrate this, the existing machine is simulated with a $\sqrt{10}$ times larger powering current, which roughly corresponds to a 10 times larger power density and a tenfold larger heat source density, reaching 18.4 MW/m^3 . The resulting temperature distribution along the winding direction is shown in Figure 12 for selected points. The highest temperature is 410 K in the center cross-section and 335 K in the overhang cross-section. Therefore, the highest temperature is still lower than the permitted average winding temperature of the “thermal class 180” of insulating materials [55]. The lowest temperature is found at the surface of the overhang, which is only 0.5 K higher than the spray temperature.

To further investigate the cooling effect, the resulting temperature at position 3, which is the hot spot of the winding, is evaluated for different current densities and heat transfer coefficients (see Figure 13). In Figure 13a, a current density between 10 and 40 A/mm^2 is considered. While a current density of 35 A/mm^2 stays within the “thermal class 180” limits, the maximum temperature of 462.9 K for 40 A/mm^2 exceeds the limits for the insulation class. In Figure 13b, the heat transfer coefficient is evaluated for sprays between 5 and 22.5 kW/Km^2 as well as for air-cooling, which reaches 0.25 kW/Km^2 . Additionally, a current density of $J = 35 \text{ A/mm}^2$ is considered, which was shown above to be the limit for the chosen machine winding. With a temperature difference from the center to the overhang of 88.6 K for air-cooling, and 84.6 K and 83.1 K for spray cooling with a heat transfer coefficient of 5 and 22.5 kW/Km^2 , respectively, the cooling behavior varies only by 5 K. However, the maximum temperature difference between the highest temperature of air and spray-cooling is around 200 K, which indicates a significant cooling effect using spray cooling. Note that the spray with a heat transfer coefficient of 5 kW/Km^2 is still within the

“thermal class 180” limits, which indicates that other spray materials can be applicable to spray cooling as well.

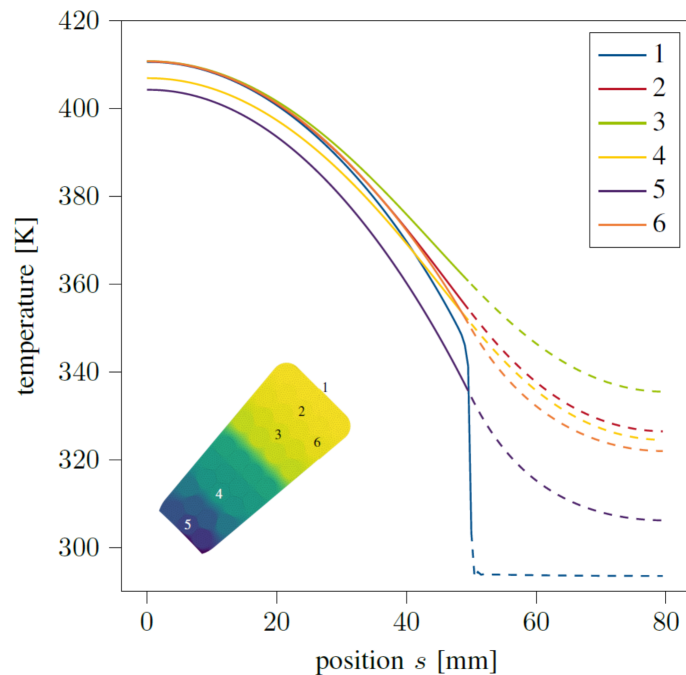


Figure 12. Temperature along the winding for a 10 times higher power density.

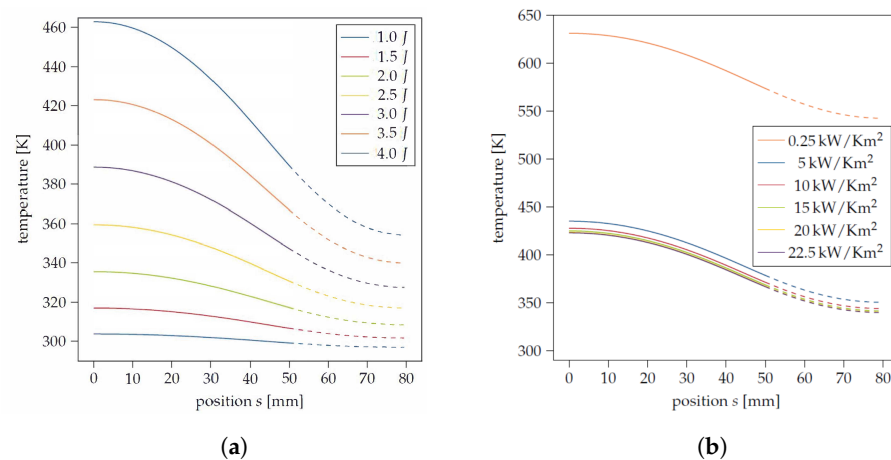


Figure 13. Temperature at position 3 along the winding direction compared for various parameters: (a) Variation of the current density. The reference current density is $J = 10 \text{ A/mm}^2$. (b) Variation of the heat transfer coefficient, for a current density of $J = 3.5 \times 10 \text{ A/mm}^2$.

7. Conclusions

In this paper, an overview of spray cooling is provided first. The necessary parameters for its description as an impedance boundary with a thermal FE model have been derived. The temperature distribution was simulated with a quasi-3D FE model, which essentially extrudes the 2D cross-sectional FE model along the winding direction to account for the heat flux from the machine’s interior to the winding overhang where spray cooling is applied. It was shown that when applying spray cooling to an initially air-rated winding model, the machine can withstand a tenfold increase in power density. Additionally, the influence of the heat transfer coefficient on the temperature distribution has been evaluated, indicating that other spray fluids may be efficient as well. Therefore, spray cooling is a promising technology for increasing the power density of electric machines.

Author Contributions: Conceptualization, H.D.G. and J.H.; Software, C.B.; Formal analysis, C.B.; Investigation, C.B. and S.A.Q.; Resources, I.V.R.; Writing—original draft, C.B. and I.V.R.; Writing—review & editing, H.D.G.; Supervision, H.D.G. and J.H.; Funding acquisition, J.H. and Y.S.-L. All authors have read and agreed to the published version of the manuscript.

Funding: This work is supported by the joint DFG/FWF Collaborative Research Centre CREATOR (DFG: Project-ID 492661287/TRR 361; FWF: 10.55776/F90, subprojects A03, A04 and B03) at TU Darmstadt, TU Graz and JKU Linz, the Graduate School Computational Engineering at TU Darmstadt, and the Athene Young Investigator Program of TU Darmstadt.

Data Availability Statement: The original contributions presented in this study are included in the article. Further inquiries can be directed to the corresponding author.

Acknowledgments: The authors would like to thank Anouar Belahcen for his valuable advice and Laura D’Angelo, Greta Ruppert, and Max Schaufelberger for their expertise in quasi-3D.

Conflicts of Interest: The authors declare no conflicts of interest.

Abbreviations

The following abbreviations are used in this manuscript:

1D	one-dimensional
2D	two-dimensional
3D	three-dimensional
BC	boundary condition
FE	finite-element
CFD	computational fluid dynamics

References

1. Rehman, Z.; Seong, K. Three-D numerical thermal analysis of electric motor with cooling jacket. *Energies* **2018**, *11*, 92. [[CrossRef](#)]
2. Fan, J.; Zhang, C.; Wang, Z.; Dong, Y.; Nino, C.; Tariq, A.; Strangas, E. Thermal analysis of permanent magnet motor for the electric vehicle application considering driving duty cycle. *IEEE Trans. Magn.* **2010**, *46*, 2493–2496. [[CrossRef](#)]
3. Chong, Y.C.; Staton, D.; Gai, Y.; Adam, H.; Popescu, M. Review of advanced cooling systems of modern electric machines for e-mobility application. In Proceedings of the 2021 IEEE Workshop on Electrical Machines Design, Control and Diagnosis (WEMDCD), Modena, Italy, 8–9 April 2021; pp. 149–154.
4. Popescu, M.; Staton, D.; Boglietti, A.; Cavagnino, A.; Hawkins, D.; Goss, J. Modern heat extraction systems for electrical machines—A review. In Proceedings of the 2015 IEEE Workshop on Electrical Machines Design, Control and Diagnosis (WEMDCD), Torino, Italy, 26–27 March 2015; pp. 289–296.
5. Konovalov, D.; Tolstorebrov, I.; Eikevik, T.M.; Kobalava, H.; Radchenko, M.; Hafner, A.; Radchenko, A. Recent Developments in Cooling Systems and Cooling Management for Electric Motors. *Energies* **2023**, *16*, 7006. [[CrossRef](#)]
6. Shams Ghahfarokhi, P.; Podgornovs, A.; Kallaste, A.; Marques Cardoso, A.J.; Belahcen, A.; Vaimann, T. The Oil Spray Cooling System of Automotive Traction Motors: The State of the Art. *IEEE Trans. Transp. Electrif.* **2023**, *9*, 428–451. [[CrossRef](#)]
7. Wang, X.; Li, B.; Huang, K.; Yan, Y.; Stone, I.; Worrall, S. Experimental investigation on end winding thermal management with oil spray in electric vehicles. *Case Stud. Therm. Eng.* **2022**, *35*, 102082. [[CrossRef](#)]
8. Farsane, K.; Desevaux, P.; Panday, P.K. Experimental study of the cooling of a closed type electric motor. *Appl. Therm. Eng.* **2000**, *20*, 1321–1334. [[CrossRef](#)]
9. Ghahfarokhi, P.S.; Kallaste, A.; Podgornovs, A.; Belahcen, A.; Vaimann, T. Development of analytical thermal analysis tool for synchronous reluctance motors. *IET Electr. Power Appl.* **2020**, *14*, 1828–1836. [[CrossRef](#)]
10. Shams Ghahfarokhi, P.; Kallaste, A.; Belahcen, A.; Vaimann, T. Analytical thermal model and flow network analysis suitable for open self-ventilated machines. *IET Electr. Power Appl.* **2020**, *14*, 929–936. [[CrossRef](#)]
11. Chen, H.; Ruan, X.h.; Peng, Y.h.; Wang, Y.l.; Yu, C.k. Application status and prospect of spray cooling in electronics and energy conversion industries. *Sustain. Energy Technol. Assess.* **2022**, *52*, 102181. [[CrossRef](#)]
12. Liu, C.; Xu, Z.; Gerada, D.; Li, J.; Gerada, C.; Chong, Y.C.; Popescu, M.; Goss, J.; Staton, D.; Zhang, H. Experimental Investigation on Oil Spray Cooling With Hairpin Windings. *IEEE Trans. Ind. Electron.* **2020**, *67*, 7343–7353. [[CrossRef](#)]
13. Hoffmann, F.; Bender, J.; Parche, M.; Wetzel, T.; Doppelbauer, M. Local Heat Transfer Coefficient Measurements on Shaft Spray Cooled End Windings. In Proceedings of the 2023 IEEE International Electric Machines & Drives Conference (IEMDC), San Francisco, CA, USA, 15–18 May 2023; pp. 1–7. [[CrossRef](#)]

14. Zhang, F.; Gerada, D.; Xu, Z.; Liu, C.; Zhang, H.; Zou, T.; Chong, Y.C.; Gerada, C. A thermal modeling approach and experimental validation for an oil spray-cooled hairpin winding machine. *IEEE Trans. Transp. Electrification* **2021**, *7*, 2914–2926. [[CrossRef](#)]
15. Zhao, A.; Duwig, C.; Liu, C.; Gerada, D.; Leksell, M. Parameter study for oil spray cooling on endwindings of electric machines via Eulerian–Lagrangian simulation. *Appl. Therm. Eng.* **2023**, *235*, 121281. [[CrossRef](#)]
16. El-Refaie, A.M.; Alexander, J.P.; Galioto, S.; Reddy, P.B.; Huh, K.K.; de Bock, P.; Shen, X. Advanced high-power-density interior permanent magnet motor for traction applications. *IEEE Trans. Ind. Appl.* **2014**, *50*, 3235–3248. [[CrossRef](#)]
17. Dong, H.; Ruan, L.; Wang, Y.; Yang, J.; Liu, F.; Guo, S. Performance of air/spray cooling system for large-capacity and high-power-density motors. *Appl. Therm. Eng.* **2021**, *192*, 116925. [[CrossRef](#)]
18. Li, Z.; Guo, J.; Fu, D.; Gu, G.; Xiong, B. Research on heat transfer of spraying evaporative cooling technique for large electrical machine. In Proceedings of the 2009 International Conference on Electrical Machines and Systems, Tokyo, Japan, 15–18 November 2009; pp. 1–4.
19. Guechi, M.R.; Désévaux, P.; Baucour, P. On the numerical and experimental study of spray cooling. *J. Comput. Multiph. Flows* **2013**, *5*, 239–249. [[CrossRef](#)]
20. Guechi, M.; Desevaux, P.; Baucour, P.; Espanet, C.; Brunel, R.; Poirot, M. Spray cooling of electric motor coil windings. *J. Comput. Multiph. Flows* **2016**, *8*, 95–100. [[CrossRef](#)]
21. Albrecht, H.E.; Damaschke, N.; Borys, M.; Tropea, C. *Laser Doppler and Phase Doppler Measurement Techniques*; Springer Science & Business Media: Berlin/Heidelberg, Germany, 2013.
22. Tropea, C. Optical particle characterization in flows. *Annu. Rev. Fluid Mech.* **2011**, *43*, 399–426. [[CrossRef](#)]
23. Mudawar, I.; Deiters, T.A. A universal approach to predicting temperature response of metallic parts to spray quenching. *Int. J. Heat Mass Transf.* **1994**, *37*, 347–362. [[CrossRef](#)]
24. Hall, D.D.; Mudawar, I. Experimental and numerical study of quenching complex-shaped metallic alloys with multiple, overlapping sprays. *Int. J. Heat Mass Transf.* **1995**, *38*, 1201–1216. [[CrossRef](#)]
25. Tilton, D.E.; Kearns, D.A.; Tilton, C.L. Liquid nitrogen spray cooling of a simulated electronic chip. In *Advances in Cryogenic Engineering*; Springer: Berlin/Heidelberg, Germany, 1994; pp. 1779–1786.
26. Yin, J.; Wang, S.; Sang, X.; Zhou, Z.; Chen, B.; Thrassos, P.; Romeos, A.; Giannadakis, A. Spray cooling as a high-efficient thermal management solution: A review. *Energies* **2022**, *15*, 8547. [[CrossRef](#)]
27. Huddle, J.J.; Chow, L.C.; Lei, S.; Marcos, A.; Rini, D.P.; Lindauer, S.J.; Bass, M.; Delfyett, P.J. Thermal management of diode laser arrays. In Proceedings of the Sixteenth Annual IEEE Semiconductor Thermal Measurement and Management Symposium (Cat. No. 00CH37068), San Jose, CA, USA, 21–23 March 2000; pp. 154–160.
28. Liu, R.; Zhang, L.; Zhang, X. Applications of spray cooling technology in aerospace field. *Proc. IOP Conf. Ser. Mater. Sci. Eng.* **2019**, *470*, 012020. [[CrossRef](#)]
29. Torres, J.H.; Nelson, J.S.; Tanenbaum, B.S.; Milner, T.E.; Goodman, D.M.; Anvari, B. Estimation of internal skin temperatures in response to cryogen spray cooling: Implications for laser therapy of port wine stains. *IEEE J. Sel. Top. Quantum Electron.* **1999**, *5*, 1058–1066. [[CrossRef](#)]
30. Zhang, T.; Mo, Z.; Xu, X.; Liu, X.; Chen, H.; Han, Z.; Yan, Y.; Jin, Y. Advanced study of spray cooling: From theories to applications. *Energies* **2022**, *15*, 9219. [[CrossRef](#)]
31. Kim, J. Spray cooling heat transfer: The state of the art. *Int. J. Heat Fluid Flow* **2007**, *28*, 753–767. [[CrossRef](#)]
32. Liang, G.; Mudawar, I. Review of spray cooling—Part 1: Single-phase and nucleate boiling regimes, and critical heat flux. *Int. J. Heat Mass Transf.* **2017**, *115*, 1174–1205. [[CrossRef](#)]
33. Breitenbach, J.; Roisman, I.V.; Tropea, C. From drop impact physics to spray cooling models: A critical review. *Exp. Fluids* **2018**, *59*, 55. [[CrossRef](#)]
34. Moreira, A.L.N.; Moita, A.S.; Pano, M.R. Advances and challenges in explaining fuel spray impingement: How much of single droplet impact research is useful? *Prog. Energy Combust. Sci.* **2010**, *36*, 554–580. [[CrossRef](#)]
35. Yarin, A.L.; Roisman, I.V.; Tropea, C. *Collision Phenomena in Liquids and Solids*; Cambridge University Press: Cambridge, UK, 2017.
36. Cossali, G.E.; Coghe, A.; Marengo, M. The impact of a single drop on a wetted solid surface. *Exp. Fluids* **1997**, *22*, 463–472. [[CrossRef](#)]
37. Mundo, C.; Sommerfeld, M.; Tropea, C. Droplet-wall collisions: Experimental studies of the deformation and breakup process. *Int. J. Multiph. Flow* **1995**, *21*, 151–173. [[CrossRef](#)]
38. van Hinsberg, N.P.; Budakli, M.; Göhler, S.; Berberović, E.; Roisman, I.V.; Gambaryan-Roisman, T.; Tropea, C.; Stephan, P. Dynamics of the cavity and the surface film for impingements of single drops on liquid films of various thicknesses. *J. Colloid Interface Sci.* **2010**, *350*, 336–343. [[CrossRef](#)] [[PubMed](#)]
39. Stumpf, B.; Hussong, J.; Roisman, I.V. Drop impact onto a substrate wetted by another liquid: Flow in the wall film. *Colloids Interfaces* **2022**, *6*, 58. [[CrossRef](#)]
40. D’Angelo, L.A.M.; Christ, J.; De Gersem, H. Quasi-3D Discretization of Thermal Hot-Spot Propagation in Superconducting Models. *IEEE Trans. Appl. Supercond.* **2020**, *30*, 1–5. [[CrossRef](#)]

41. Wen, T.; Luo, Y.; He, W.; Gang, W.; Sheng, L. Development of a novel quasi-3D model to investigate the performance of a falling film dehumidifier with CFD technology. *Int. J. Heat Mass Transf.* **2019**, *132*, 431–442. [[CrossRef](#)]
42. Liu, C.; Ruan, J.; Wen, W.; Gong, R.; Liao, C. Temperature rise of a dry-type transformer with quasi-3D coupled-field method. *IET Electr. Power Appl.* **2016**, *10*, 598–603. [[CrossRef](#)]
43. Driendl, N.; Pauli, F.; Hameyer, K. Influence of Ambient Conditions on the Qualification Tests of the Interturn Insulation in Low-Voltage Electrical Machines. *IEEE Trans. Ind. Electron.* **2022**, *69*, 7807–7816. [[CrossRef](#)]
44. Eickhoff, H.T. Fault-Tolerant Operation of Three-Phase Squirrel Cage Induction Machine Drives after Inverter Open Circuit Faults. Ph.D. Thesis, Graz University of Technology, Graz, Austria, 2020.
45. Bergfried, C.; Späck-Leigsnering, Y.; Seebacher, R.; Eickhoff, H.; Muetze, A. Thermal finite element modeling and simulation of a squirrel-cage induction machine. *Int. J. Appl. Electromagn. Mech.* **2024**, *76*, 147–160. [[CrossRef](#)]
46. Blumrich, L.; Bergfried, C.; Galetzka, A.; De Gerssem, H.; Seebacher, R.; Mütze, A.; Späck-Leigsnering, Y. Thermal Model Calibration of a Squirrel-Cage Induction Machine. In Proceedings of the 2024 International Conference on Electrical Machines (ICEM), Torino, Italy, 1–4 September 2024; pp. 1–7. [[CrossRef](#)]
47. VDI e.V. *VDI Heat Atlas*; Springer: Berlin/Heidelberg, Germany, 2010.
48. Bundschuh, J.; Ruppert, M.G.; Späck-Leigsnering, Y. Pyrit: A Finite Element Based Field Simulation Software Written in Python. *COMPEL* **2023**, *42*, 1007–1020. [[CrossRef](#)]
49. COMSOL Multiphysics, Stockholm, Sweden. Adapted by HDG. Available online: www.comsol.com (accessed on 19 December 2024).
50. Meschede, D.; Gerthsen, C. *Gerthsen Physik*; Springer-Lehrbuch; Springer: Berlin/Heidelberg, Germany, 2015.
51. Fletcher, C.A.J., Galerkin Finite-Element Methods. In *Computational Galerkin Methods*; Springer: Berlin/Heidelberg, Germany, 1984; pp. 86–154. [[CrossRef](#)]
52. Paloschi, D.; Bronnikov, K.A.; Korganbayev, S.; Wolf, A.A.; Dostovalov, A.; Saccomandi, P. 3D Shape Sensing With Multicore Optical Fibers: Transformation Matrices Versus Frenet-Serret Equations for Real-Time Application. *IEEE Sens. J.* **2021**, *21*, 4599–4609. [[CrossRef](#)]
53. Kyriopoulos, O.N. Gravity Effect on Liquid Film Hydrodynamics and Spray Cooling. Ph.D. Thesis, Technische Universität Darmstadt, Darmstadt, Germany, 2010.
54. Gambaryan-Roisman, T.; Kyriopoulos, O.; Roisman, I.; Stephan, P.; Tropea, C. Gravity effect on spray impact and spray cooling. *Microgravity Sci. Technol.* **2007**, *19*, 151–154. [[CrossRef](#)]
55. Pyrhönen, J.; Jokinen, T.; Hrabovcová, V. *Design Rotating Electrical Machines*; John Wiley & Sons: Hoboken, NJ, USA, 2013.

Disclaimer/Publisher’s Note: The statements, opinions and data contained in all publications are solely those of the individual author(s) and contributor(s) and not of MDPI and/or the editor(s). MDPI and/or the editor(s) disclaim responsibility for any injury to people or property resulting from any ideas, methods, instructions or products referred to in the content.